An improved hydromechanical model for particle flow simulation of fractures in fluid-saturated rocks

Yulong Zhang, Jianfu Shao, Zaobao Liu, Chong Shi

Version of Record: https://www.sciencedirect.com/science/article/pii/S1365160921002549
Manuscript_56922501c7ce692365a4e350bd8c34f0

An improved hydromechanical model for particle flow simulation of fractures in fluid-saturated rocks

Yulong Zhang[a], Jianfu Shao[a,b,*], Zaobao Liu[c], Chong Shi[a]

[a]*Key Laboratory of Ministry of Education for Geomechanics and Embankment Engineering, Hohai University, Nanjing, 210098 China*
[b]*University of Lille, CNRS, Centrale Lille, UMR9013, LaMcube, 59000 Lille, France*
[c]*Key Laboratory of Ministry of Education on Safe Mining of Deep Metal Mines, College of Resources and Civil Engineering, Northeastern University, Shenyang, 110819, China*

Abstract

Fracture initiation and propagation in fluid-saturated rocks are controlled by interaction between fluid flow and rock deformation. The description of hydromechanical coupling is essential for modeling the fracture process. In this paper, an improved hydromechanical model is proposed in the framework of the particle flow simulation method. This model provides a better description of hydraulic properties before and after breakage of bonds and can efficiently describe fluid flow through porous rock matrix and along fractures. The efficiency of the proposed model is first assessed by comparisons with analytical solutions and typical experimental evidences. A series of numerical simulations are then realized to investigate effects of some key parameters such as confining stress, fluid injection rate and viscosity on the initiation and propagation of fractures.

Keywords: Fracture, porous rocks, hydromechanical coupling, particle flow simulation, discrete element method

1. Introduction

Initiation and propagation of cracks or fractures are the principal failure mechanism of rock-like materials. The description of fracturing process is crucial for many engineering applications including stability and safety of structures and exploitation of un-conventional natural resources such as geothermal energy (Pruess, 2006; Warpinski et al., 2009). When rocks are saturated by fluids, the fracturing process can be driven by multiple processes such as stress variation, fluid pressure evolution, chemical and physical dissolution of minerals in rocks, ans convective transport of fluid and heat. It is thus needed to take into account these mechanical-physical and chemical interactions in modeling of fracturing. However, the present study focuses on hydromechanical coupling process.

During the last decades, significant advances have been achieved on numerical modeling of cracking and fracturing by the development of different kinds of computer methods and codes. Many of

*Corresponding author: jian-fu.shao@polytech-lille.fr

them are based on the concepts of continuum mechanics and the objective is to account for displacement discontinuities across fractures. As representative examples, we can mention here the enriched finite element methods (EFEM) by considering the displacement discontinuities at the elementary level with the help of enriched shape functions (Oliver, 1996). Differently, the global nodal enrichment techniques have been introduced in the extended finite element methods (XFEM) (Moes et al., 1999). This method was successively applied to modeling hydraulic fracturing in saturated rocks (Zeng et al., 2018, 2019). More recently, based on the variational principle (Francfort and Marigo, 1998) and the optimal approximation methods of functionals with jumps (Ambrosio and Tortorelli, 1990; Mumford and Shah, 1989; Bourdin et al., 2000), the so-called phase-field method has been rapidly developed for modeling the transition from diffuse damage to localized cracks in elastic materials under both static and dynamic loads (Miehe et al., 2010; Borden et al., 2012; Ambati et al., 2015) and plastic materials (Fang et al., 2019; Choo and Sun, 2018). The phase-field method has also been applied to multi-physics coupling problems (Miehe et al., 2015).

As alternative solutions to those continuum mechanics based approaches, different kinds of discrete element methods have also been developed. Among them, the particle flow method is one of the widely used (Cundall, 2008; Potyondy and Cundall, 2004; Shimizu et al., 2011). In this method, the grain-scale micro-structures of rocks are represented by an assembly of particles and voids. The particles are bonded. The macroscopic deformation and failure are inherently related to the local behavior of bonds. Bonds also play the role of hydraulic pipes. Fluid flow occurs between voids and through open pipes. Macroscopic hydraulic properties are intimately dependent on the aperture of microscopic pipes. Therefore, the description of hydraulic aperture of pipes is a crucial issue for hydromechanical modeling with the particle flow method. A number of previous studies have been reported on modeling of hydraulically driven fractures with the particle flow method, for instance (Al-Busaidi et al., 2005; Zhao, 2010; Shimizu et al., 2011; Damjanac and Cundall, 2016; Zhou et al., 2016). In addition, the particle simulation method was also applied to investigating magma-intrusion induced cracks (Zhao et al., 2007, 2008a) and other types of large-scale cracking problems inside the upper crust of the Earth (Zhao et al., 2009). Therefore, this method can find many applications in the emerging field of computational geosciences. However, in most previous studies, a very simple model originally embedded in the particle flow code (PFC) (Cundall, 2008) was used to describe fluid flow. In particular, the hydraulic aperture of pipes was defined as a linear function of normal contact force. That model was not able to differentiate the aperture evolution between bonds under compression and tension, and between unbroken and broken bonds. As a consequence, in many previous studies, the authors have generally focused on final fracture patterns only without giving detailed fracturing progress steps such as the initiation, breakdown and break-through (Eshiet et al., 2013; Wang et al.,

2014; Fatahi et al., 2017; Wang et al., 2017).

On the other hands, a number of experimental studies have also been conducted (Jian et al., 2010; Goodfellow et al., 2015). In particular, some works were devoted to investigating effects of key parameters which could affect fracture process, such as fluid injection rate (Zoback et al., 1977; Bohloli and de Pater, 2006), confining stress (Zhou et al., 2008; Nazari Moghaddam and Jamiolahmady, 2016) and fluid viscosity (Ishida et al., 2004; Zhang et al., 2017). Some results have indicated that the fracture breakdown could be influenced by fluid injection rate. The fluid infiltration rate controlled by fluid viscosity could also have some influences on fluid pressure evolution and fracture patterns. Obviously, the influences of such parameters should be taken into account in modeling of hydraulically driven fracture process. Moreover, it should be pointed out that, some chemical-physical dissolution processes (Zhao et al., 2008b, 2010) as well as convective transport of pore-fluid and heat (Zhao et al., 2008c) may also induce initiation and propagation of cracks in rocks such as well-known fingers and wormholes. This kind of instability problems generally involves interactions among the mechanical loading, pore-fluid flow and mass transport and chemical-physical reactions. But, the description of all these interactions in modeling cracking process by the particle simulation based method is a delicate task and remains an open issue. Further advances are still needed.

In this paper, a new hydromechanical model is proposed in the framework of particle flow method to better capture the fluid flow through porous rock matrix and along fractures. For this purpose, the variation of hydraulic aperture of pipes is differently described for bonds under tension and compression, and for unbroken and broken bonds. Further, the fluid pressure balance between two neighboring void domains due to bond breakage is also taken into account. The proposed model is implemented into the PFC code, and is assessed through comparisons with analytical solutions and typical experimental evidences. A series of numerical simulations are performed in order to investigate effects of confining stress, fluid injection rate and viscosity on pressure responses and fracturing patterns. Compared with most continuum-mechanics based models, the particle flow method provides some physical links between local breakage of bonds and macroscopic fracturing, and has the advantage to easily describe complex scenarios of multiple fractures.

The following sign convention will be adopted throughout the paper. The compressive normal contact force is denoted as positive and the tensile one as negative. However, the normal opening (aperture) is denoted as positive and the closure as negative.

2. An improved hydromechanical coupling model

In the framework of particle flow simulation, cohesive porous rocks are represented by an assembly of discrete particles which are connected by bonded interfaces. Voids are distributed along

particles. The overall deformation and failure of rocks are driven by the local behavior of interfaces (or bonds). The basic features of particle flow simulation have been presented in many previous publications (Potyondy and Cundall, 2004; Cundall, 2008; Zhao et al., 2009). In this section, the emphasis is put on the formulation of a hydromechanical model for fluid-saturated porous rocks.

2.1. Elastic behavior of contact

When the local contact forces are small, the mechanical behavior of a bond is described by the following linear elastic model:

$$\Delta F_n = -k_n \Delta u_n^e \tag{1}$$

$$\Delta F_s = k_s \Delta u_s \tag{2}$$

where F_n and F_s are the normal and shear contact forces. k_n and k_s denote the local elastic stiffness along the normal and shear directions. It is worth noticing that the values of local elastic stiffness can evolve with the values of contact forces leading to a nonlinear elastic behavior. More details can be found in (Zhang et al., 2018).

2.2. Contact failure criterion

It is assumed that the contact interfaces of cohesive rocks are initially bonded and progressively broken when the local forces reach the critical values. Both tensile (or normal) and shear failure mechanisms are here considered and illustrated in Figure 1. The tensile failure occurs when the normal contact force (negative sign for tensile force) reaches the corresponding tensile strength $F_n = \varphi_{nt}$. For the shear failure, due to the roughness of contact interfaces, it is assumed that a residual shear strength exists after breakage. Therefore, the shear strength of a contact is described by two envelopes, respectively corresponding to the peak and residual shear strength. Further, in order to better describe the effect of compressive normal force on the shear strength, a bi-linear criterion has been proposed in our previous work (Zhang et al., 2018). This criterion is adopted in the present study. For the sake of simplicity, it is assumed that the contact breakage is entirely represented by the full destruction of cohesion. However, the frictional coefficients are kept unchanged. More precisely, the peak and residual strength envelops are respectively described by the following relations:

$$F_s = \begin{cases} 0 & , \ F_n < \varphi_{nt} \\ \varphi_s + F_n \tan\phi_1 & , \ \varphi_{nt} \le F_n \le \varphi_{ncr} \\ \varphi_s + \varphi_{ncr}(\tan\phi_1 - \tan\phi_2) + F_n \tan\phi_2 & , \ F_n \ge \varphi_{ncr} \end{cases} ; \ \text{peak shear strength} \tag{3}$$

$$F_s = \begin{cases} 0 & , \ F_n \le 0 \\ F_n \tan\phi_1 & , \ 0 < F_n \le \varphi_{ncr} \\ \varphi_{ncr}(\tan\phi_1 - \tan\phi_2) + F_n \tan\phi_2 & , \ F_n > \varphi_{ncr} \end{cases} ; \ \text{redisual shear strength} \tag{4}$$

In these relations, φ_1 is the frictional coefficient for the low normal force regime while ϕ_2 is that for the high normal force regime. φ_{ncr} denotes the characteristic transition value of normal force between the two regimes. In general, under a high normal compression, asperities of contact surfaces can be destroyed. As a consequent, the frictional coefficient is reduced. Thus, one gets $\phi_2 < \phi_1$.

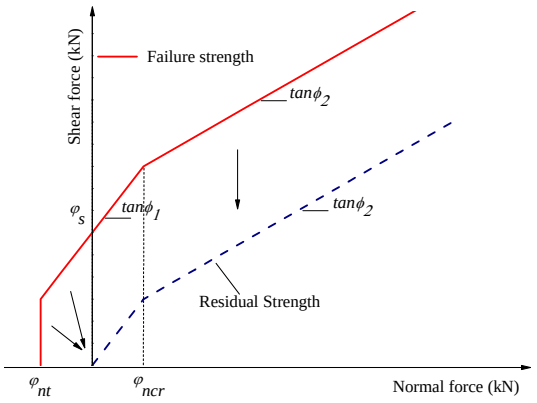

Figure 1: Peak and residual strength envelopes of bonded contacts

2.3. *Fluid flow model*

In the framework of particle flow simulation, the fluid flow occurs through voids and channels (or pipes) between particles, as illustrated in Fig. 2. Each pipe is characterized by its length and aperture. A fictive domain is created around a pore by connecting the centers of all surrounding particles, as shown by the red lines in the figure. When there is a pressure gradient between two adjacent domains, the fluid flow takes place through the pipe connecting these domains. Assuming that the fluid flow verifies the Poiseuille law and by taking the unit out-of-plane thickness, the fluid flow rate q (in m^2/s) is given by:

$$q = \frac{e^3(p_1 - p_2)}{12\mu L_p} \tag{5}$$

where e and L_p are the hydraulic aperture and length of pipe. μ is the fluid viscosity and $p_1 - p_2$ denotes the pressure difference between two domains. Accordingly, the fluid pressure variation inside the domain during a time increment Δt can be calculated by:

$$\Delta p = \frac{K_f}{V_d}(\sum q\Delta t - \Delta V_d) \tag{6}$$

K_f is the bulk modulus of fluid, V_d and ΔV_d denote the domain volume and its variation. The impact of fluid pressure on mechanical deformation is described by calculating the equivalent body forces applied onto the surrounding particles, as illustrated in Fig. 2(c). The mechanical deformation modifies the aperture of pipes and thus the hydraulic properties. Therefore, the fluid flow and mechanical deformation are coupled and their coupling is described below.

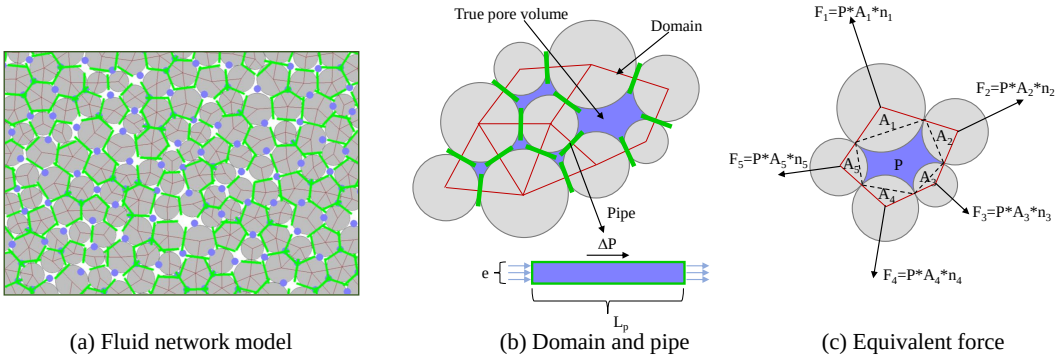

(a) Fluid network model (b) Domain and pipe (c) Equivalent force

Figure 2: Fluid flow model: solid particles (gray circles), flow channels (green lines), domains (red polygons) and domain's centers (blue points)

2.4. An improved hydraulic aperture law

As mentioned above, the fluid flow through a pipe is directly controlled by its aperture. Therefore, it is crucial to describe the evolution of pipe aperture during the mechanical deformation process. In classical particle flow simulation, a common model (CM) is widely adopted. The pipe aperture is expressed as a linear function of normal contact force as follows:

$$e = \frac{e_{ini} F_n^0}{F_n + F_n^0} \tag{7}$$

where e_{ini} denotes the initial aperture. F_n^0 is the reference normal force at which the aperture is reduced to the half of its initial value.

On the other hand, according to a large number of experimental studies (Worthington, 2008; Zisser and Nover, 2009; Nazari Moghaddam and Jamiolahmady, 2016), the overall permeability of porous rocks generally exhibits a non-linear dependency on applied confining stress and depends on cracking process. As the overall permeability is inherently related to the local hydraulic aperture of pipes, an improved empirical law (called the IM model) is here proposed to describe the evolution of pipe aperture as a non-linear function of normal contact force and bond breakage state. This is expressed by the following relations:

$$e = \begin{cases} e_{res} + (e_{ini} - e_{res}) \exp(-\alpha F_n) \ , & \text{compressive normal force} \\ e_{ini} + \beta \Delta d \ , & \text{tensile normale force or broken bond} \end{cases} \tag{8}$$

e_{ini} and e_{res} denote the initial and residual aperture of pipe respectively. Δd is the distance between two adjacent particles. α and β are two parameters controlling the evolution of hydraulic aperture of a pipe.

In addition, when a contact bond is broken, there is an instantaneous fluid diffusion between two adjacent domains. This process is not taken into account in the classical model. In the improved model, the instantaneous diffusion process is described by the reallocation of fluid pressure between

two adjacent domains. More precisely, when the bond is intact, the hydraulic aperture of the corresponding pipe evolves with the normal force according to the relations (8). Once the bond breakage occurs, the fluid pressure in two adjacent domains is simultaneously reallocated to p'_f as follows:

$$p'_f = \frac{p_1 + p_2}{2} \tag{9}$$

During the subsequent time steps, due to the fluid change between other domains, the values of fluid pressure become again different in the two adjacent domain. The aperture of broken pipe between them is calculated by the second relation of (8). It is worth noticing that the consideration of such fluid-pressure balance due to bond breakage allows the description of instantaneous or rapid change of fluid pressure due to growth of fractures. As a consequence, compared with the classical one, the improved hydromechanical model is expected to provide a better description of fluid pressure evolution which drives the propagation of hydraulically induced fractures. This feature will be illustrated below through different numerical simulations.

3. Calibration and assessment of model's parameters

The improved hydromechanical model is implemented in the standard Particle Flow Code (PFC). In this section, the calibration of parameters involved in the model is first discussed. Effects of some main parameters on hydraulically driven fracturing are assessed through representative numerical simulations.

3.1. Calibration of mechanical parameters

The mechanical parameters involved in the particle flow method include the elastic stiffness coefficients (k_n, k_t), frictional angles (ϕ_1, ϕ_2), normal tensile strength (φ_{nt}), shear strength (φ_s) and transition normal force (φ_{ncr}). There are some empirical relations between the bond elastic stiffness coefficients and macroscopic elastic properties (Zhao et al., 2009; Zhang et al., 2018, 2019). These relations allow providing the trial values of k_n and k_t. However, for the complete identification of elastic and failure parameters, an iterative optimization procedure is requested, based on numerical simulations of typical laboratory tests. For instance, uniaxial compression and tension are widely used. For this propose, a rectangular numerical sample of 150mm in width and 300mm in height is here adopted. It is constituted by 10000 particles with an average radius of 1.33mm. The choice of particle size and distribution is based on previous studies and allows reducing its effect on mechanical response as smaller as possible (Zhang et al., 2018).

During the iterative optimization, the elastic stiffness coefficients are calibrated on the linear part of stress-strain curves. The failure parameters are optimized with respect to the peak stresses in compression and tension tests. In the present study, the calibration is mainly based on the experimental

data reported in (Sarmadivaleh and Rasouli, 2015). The obtained values of parameters are given in Table 1. In Figure 3, one can see the comparison between numerical and experimental results in an uniaxial compression test. Unfortunately, no experimental data of uniaxial tension test are available for the same rock, only numerical simulation is presented here. In this figure, the failure modes in two tests are also illustrated. Under the uniaxial compression, multiple cracks are created and the failure is caused by several inclined fractures. In the uniaxial tension test, a single horizontal fracture is observed and leads to the sample failure. These failure patterns correspond well to experimental observations of rock-like materials (Sarmadivaleh and Rasouli, 2015). However, the ratio of uniaxial compression and tension strength obtained the numerical results ranges form 4 and 5. This value is clearly lower than that commonly observed for most rocks, say between 10 and 20. Such a difference represents an important shortcoming (or limitation) of the particle simulation based method. More precisely, a numerical sample composed of randomly distributed particles and contact surfaces is used in our simulations of uniaxial compression and tension tests. Under the macroscopic uniaxial tension, only the horizontally oriented contact surfaces are subjected to tensile force, but the others to tangential shear force. Therefore, the macroscopic tensile strength is not only controlled by the microscopic tensile strength but also the shear one of bonds. As a consequence, it is generally difficult to obtain a large ratio of uniaxial compression and tension strength even using a very small value of microscopic tensile strength φ_{nt}. In order to reproduce such a high compression-tension strength difference, it is needed to use specific samples containing preferentially oriented contact surfaces or weakness bonds. This aspect is not discussed in the present work.

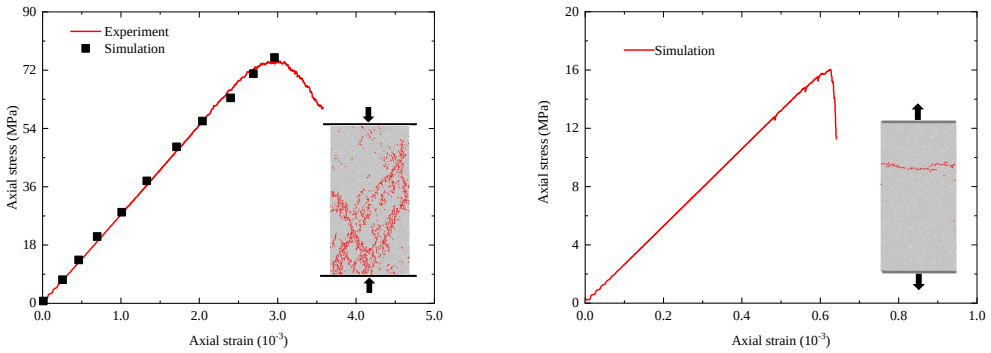

(a) Uniaxial compression test (b) Direct tension test

Figure 3: Typical mechanical responses and failure patterns of rocks under uniaxial compression and tension tests

3.2. Determination of hydraulic aperture

The improved hydromechanical coupling model presented in the relations (8) contains four parameters, namely the initial aperture e_{ini}, the residual aperture e_{res} and two coefficients controlling the evolution of aperture α and β. The following procedure is adopted for the determination of these

parameters. The values of e_{ini} and e_{res} are first determined from macroscopic permeability while those of α and β are calibrated subsequently from sensitivity studies.

Indeed, the fluid flow property of porous media is characterized by the value of permeability k at the macroscopic scale while equivalently by the hydraulic aperture of pipes at the microscopic scale. However, the equivalence principle of fluid flow rate described by two approaches can be used to establish the relationships between the macroscopic permeability and microscopic pipe aperture. Inspired by the previous work reported in (Zhou et al., 2016), the following empirical relation is adopted to obtain the first approximation of initial (or residual) value of hydraulic pipe aperture:

$$k_{ini(res)} = \frac{1}{12V} \sum_{pipe} L_p e^3_{ini(res)} \tag{10}$$

where V is the total volume of the studied domain, L_p is the average length of pipes. It is worth noticing that the approximate values calculated from this relation are further refined by comparing numerical and experimental results in the representative fluid flow tests. The typical values used in this study are presented in Table 1.

3.3. Assessment and identification of parameter α

Parameter α controls the evolution of pipe aperture with the compressive normal contact force, as described by the first equation of (8). There is no way to determine its value directly from measurable macroscopic data. Therefore, the value of α is indirectly estimated from the variation of macroscopic permeability with confining stress. For this purpose, a series of numerical simulations of fluid flow are first performed by using the different values of α and confining pressure. The numerical sample is a square plate of 300 mm in width and height as shown in Fig. 4(a). Fluid is injected from the left side by prescribing a pressure of $P_{in} = 1$ MPa inside a narrow band of 20 mm, and exited by the right side where the fluid pressure is kept to zero ($P_{out} = 0$) in a narrow band of 20 mm as illustrated in Fig. 4(b). When the steady-state flow is established, the fluid flow rate can be related to the pressure gradient by using the Darcy's law:

$$q_s = \frac{k}{\mu} \frac{(P_{in} - P_{out})}{W} \tag{11}$$

q_s denotes the steady-state flow rate per unit area. μ is the fluid viscosity and $W = 260$ mm the effective flow length. Depending on the value of permeability, the time needed to reach the steady-state flow can be more or less long. For the sake of simplicity, it is commonly adopted that the stabilized values of inflow rate can be used as the steady-state flow rate such as reported in previous studies (Al-Busaidi et al., 2005; Shimizu et al., 2011). This value is then used for the estimation of average macroscopic permeability k. In Fig. 4(d), one shows the variation of macroscopic permeability with applied confining stress ($\sigma_x = \sigma_y$), for different values of α and with $\mu = 1.0 \cdot 10^{-3}$ Pa.s. The initial

and residual apertures of pipes are respectively taken as $e_{ini} = 1.0 \cdot 10^{-5}$ m and $e_{res} = 1.0 \cdot 10^{-6}$ m. It is clearly found that the macroscopic permeability rapidly decreases with the increase of confining stress during the first stage and then tends toward a stationary value which is related to the residual value of pipes aperture. Considering the numerical results obtained with the value of $\alpha = 2.0 \cdot 10^{-5}$ are quite close to the experimental observation on a shale rock (Nazari Moghaddam and Jamiolahmady, 2016), this value is taken for the subsequent simulations of the present paper.

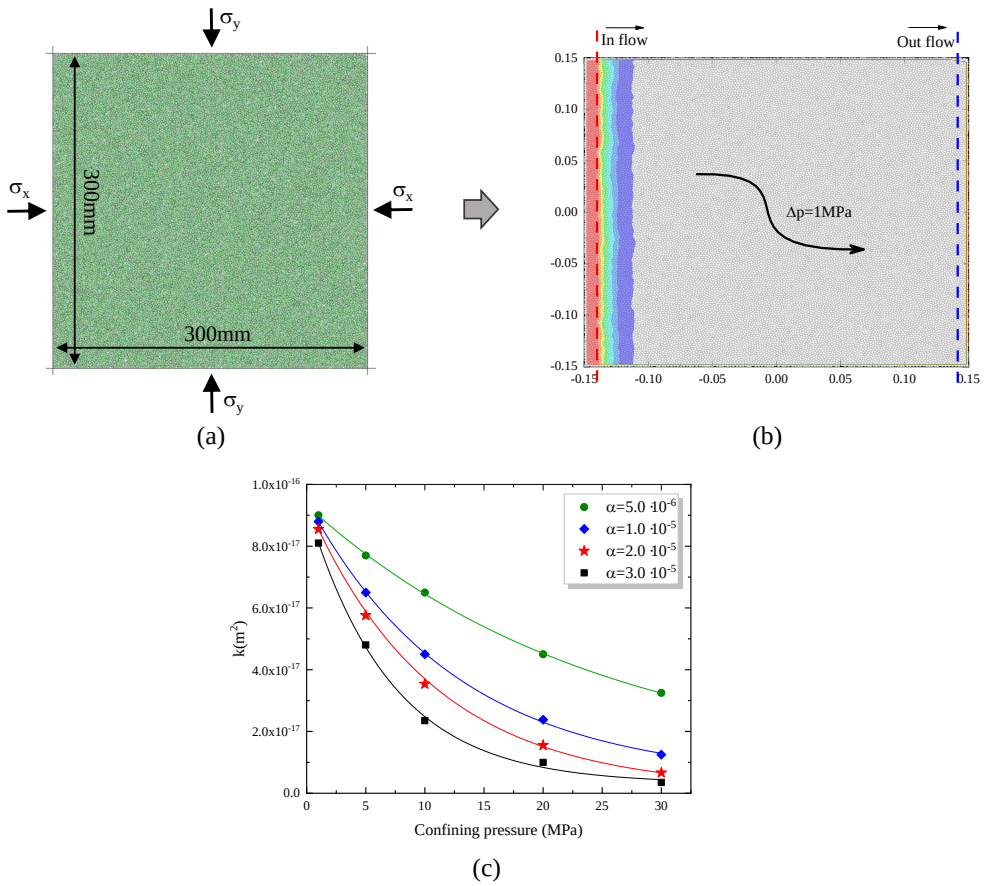

Figure 4: Numerical simulations of fluid flow with different values of α and confining stresses: (a) Numerical sample; (b) Flow boundary conditions; (c) Variation of permeability versus confining stress

3.4. Influence and identification of parameter β

In the improved hydromechanical model (8), in addition to the parameter α which controls the variation of hydraulic aperture under compressive normal force before bond breakage, the parameter β determines the hydraulic pipe aperture under tensile normal force or after the breakage of bond. Therefore, its value should directly affect the fluid pressure evolution during propagation of fracture. As for α, its value cannot be determined directly from measurable data. It is calibrated from numerical simulations of typical hydraulic patterns. In this paper, we consider the common case of hydraulic fracturing around a circular borehole due to fluid injection, as shown in Fig. 5. This case has been widely investigated in previous works. The fluid injection pressure on the borehole shows some

characteristic stages. More precisely, after an almost linear increase phase, the critical pressure P_i defines the initiation and propagation of micro-cracks. The peak value P_b is called the breakdown pressure which indicates the onset of macroscopic fractures. The post-peak values P_p and P_t define two different propagation stages of fractures. The pressure decrease after P_t indicates the creation of a large fractured zone which is generally called as the fracture break-through. The value of P_i is mainly controlled the elastic stiffness coefficients, initial pipe aperture and parameter α. However, those of P_b and P_p are directly related to the hydraulic properties of broken bonds and thus influenced by the value of β. In order to quantify its influences, a series of simulations are performed with different values of β on a square plate containing a circular borehole at its center as shown in Fig. 5. The confining stresses in the horizontal and vertical directions are fixed to 10 MPa.

The evolution of borehole pressure with time is presented in Fig. 5(b) for four values of β. As expected, the value of P_i seems not affected by β while those of P_b, P_p and P_t are significantly influenced by β. For instance, when $\beta = 0.1$, the borehole pressure almost continuously increases and it is not easy to identify the values of P_p and P_t. For $\beta = 0.9$, the borehole pressure decreases quickly after its peak value P_b. Therefore, the proposed improved hydromechanical model is able to describe the different scenarios of borehole pressure evolution. In Fig. 5(c) and Fig. 5(d), one also shows the fracture patterns around the borehole for two values of β. It is observed that when the value of β is small, the hydraulic aperture of broken bonds is reduced and the fluid flow through the pipes is lowered. A large concentration band of high fluid pressure can be created around the borehole, leading to a thick fracture or multiple fractures, as shown in Fig. 5(c). In contrary, for a high value of β, the hydraulic aperture of pipes is amplified and the fluid flow is enhanced. This leads to the quick decrease of borehole pressure after the breakdown pressure and the propagation of a fine single fracture, as presented in Fig. 5(d). Compared with the typical variation of borehole pressure obtained in previous studies (Sarmadivaleh and Rasouli, 2015; Duan et al., 2018), it seems that for the improved model proposed here, the value of β is ranged in 0.3-0.6. For the subsequent simulations, the value of β is taken as 0.5. The retained values of parameters for the subsequent simulations are summarized in Table 1. It is worth noticing that most rocks are heterogeneous materials with different types of mineral components and pores. The macroscopic mechanical and hydraulic properties of rocks are affected by such heterogeneous micro-structures. In the present study, this feature is not investigated and the assumption of homogeneous rocks is adopted. However, in the framework of particle simulation based method, there is no fundamental difficulty to take into account such a material heterogeneity. For instance, based on suitable microscopic observations, one can introduce different values of mechanical and hydraulic parameters of bonds and pipes in different zones to represent the material heterogeneity. The effect of material heterogeneity on hydraulically induced cracking process in rocks will be

220 investigated in future studies.

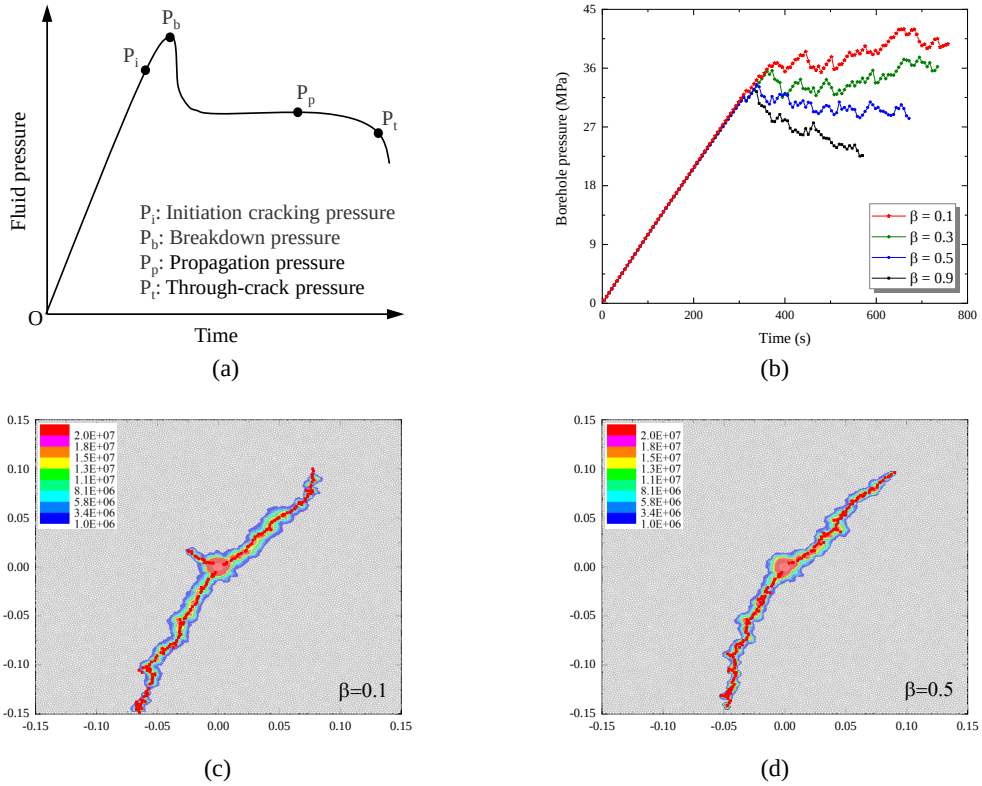

Figure 5: Simulation of hydraulic fracturing around a circular borehole in a square plate subjected to a confining stress of 10 MPa: text(a) typical stages of borehole pressure evolution during fluid injection; (b) evolution of borehole pressure with time for different values of β; (c) and (d) fluid pressure distributions respectively for $\beta = 0.1$ and 0.5, used here to illustrate fracturing patterns, localized fractures are represented by fluid pressure concentration bands

Table 1: Mechanical and hydraulic parameters used in numerical simulations

Mechanical parameters			
Normal elastic stiffness (N/m)	k_n		7.6×10^8
Shear elastic stiffness (N/m)	k_s		5.1×10^8
Friction coefficient for low stress regime	$tan\phi_1$		1.5
Friction coefficient for high stress regime	$tan\phi_2$		0.5
Tensile failure strength (N)	φ_{nt}		5.3×10^4
Shear failure strength (N)	φ_s		2.1×10^5
Transition normal stress (N)	φ_{ncr}		4.2×10^5
Calibration results		**Experiment**	**Simulation**
Uniaxial compression strength (MPa)	σ_c	73 ± 5	73.6
Uniaxial tensile strength (MPa)	σ_t	-	16.3
Young's modulus (GPa)	E	27	26.8
Poisson's ratio	ν	0.2	0.21
Hydraulic aperture parameters of pipes			
Initial hydraulic aperture (m)	e_{ini}		1.5×10^{-6}
Residual hydraulic aperture (m)	e_{res}		0.15×10^{-6}
Aperture variation parameters	α, β		2.0×10^{-5}, 0.5
Bulk modulus of fluid (GPa)	K_f		2.0
Fluid viscosity (Pa.s)	μ		$7.5.10^{-4}$
Calibration results		**Experiment**	**Simulation**
Macroscopic permeability (m^2)	k	1.0×10^{-17}	1.3×10^{-17}

4. Validation and assessment of the improved model

In this section, the improved hydromechanical model (IM) is assessed through comparisons with analytical solutions and the numerical results obtained with the common model (CM).

For this purpose, we consider here a typical case of hydraulically driven fracture around a borehole. A squared sample of 300mm in width and 300mm in height is considered and shown in Fig. 6. A circular borehole of 15mm in diameter is placed at the center of sample. This one is composed of 20000 uniformly distributed particles with an average radius of 1.33mm. It is noticed that in particle simulations, a continuous porous medium is replaced by an assembly of particles and voids. In order to reproduce the circular hole as best as possible, regularly-organized particles are placed around the borehole. The average diameter of these particles should be as small as possible. A good compromise found here between geometrical accuracy and computing facility is to used a diameter of 1 mm. The external boundary is constituted of four moving walls allowing applying desired confining stress or displacement in horizontal and vertical directions. Between the boundary and porous material region,

impermeable particles without void domains and hydraulic pipes are added inside a narrow zone to the rubber or jacket surrounding the sample in a laboratory test. In addition, in order to obtain quantitative distribution of stresses inside the discrete system, 24 and 16 stress measurement circles are identified, respectively along the circumferential and horizontal direction. More details are shown in Fig. 6(a) and (b).

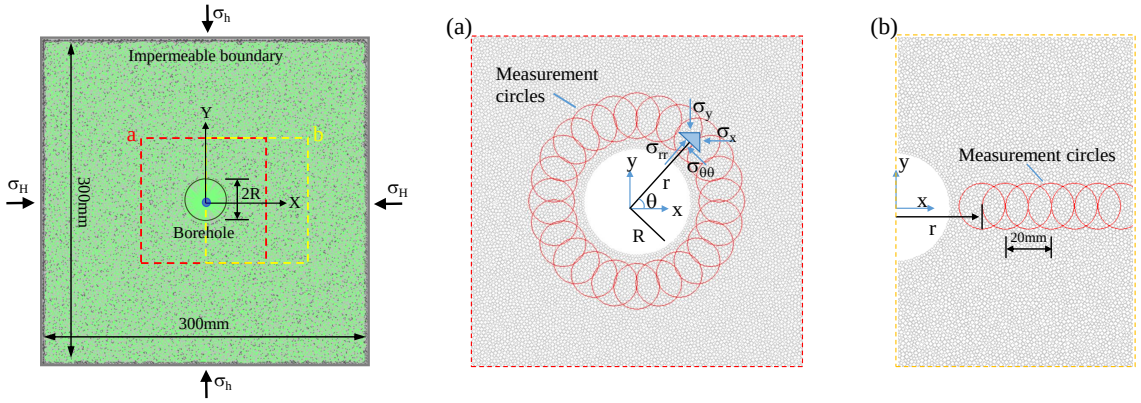

Figure 6: Geometry and boundary conditions of numerical sample: (a) distribution of circles for stress measurement along circumferential direction; (b) distribution of circles for stress measurement along horizontal direction

4.1. Verification of stress distribution

In the case of a circular injection borehole in a linear elastic and isotropic medium, the stress state before crack initiation has been studied in many previous works (Kirsch, 1898; Zoback et al., 1977; Haimson and Cornet, 2003; Haimson, 2007). The stress state can be determined by the following relations:

$$\sigma_{rr} = \frac{\sigma_H + \sigma_h}{2}(1 - \frac{R^2}{r^2}) + \frac{\sigma_H - \sigma_h}{2}(1 - 4\frac{R^2}{r^2} + 3\frac{R^4}{r^4})cos2\theta + \Delta p\frac{R^2}{r^2} \tag{12}$$

$$\sigma_{\theta\theta} = \frac{\sigma_H + \sigma_h}{2}(1 + \frac{R^2}{r^2}) - \frac{\sigma_H - \sigma_h}{2}(1 + 3\frac{R^4}{r^4})cos2\theta - \Delta p\frac{R^2}{r^2} \tag{13}$$

$$\sigma_{r\theta} = \frac{\sigma_H - \sigma_h}{2}(1 + 2\frac{R^2}{r^2} - 3\frac{R^4}{r^4})sin2\theta \tag{14}$$

σ_H and σ_h are respectively the major and minor principal far-field stresses, R is the radius of borehole. Δp denotes the fluid injection pressure. We consider here the particular case of isotropic far-stress by taking two different values, namely $\sigma_H = \sigma_h$= 5 MPa and 20 MPa. The prescribed fluid injection rate is $1{\cdot}10^{-5}$ m^3/s. In Fig. 7, the distributions of three stress components respectively along the circumferential and horizontal directions are presented when the injection pressure is equal to 30 MPa. The numerical results obtained from the common and improved models are compared with the analytical solutions. A global good agreement is obtained. Some scatters are observed for the tangential stress along the circumferential direction.This can be related to the fact that the numerical

results are calculated from the selected stress circles and can depend on the number (or size) of circles. Furthermore, for these elastic cases, the differences between two numerical models are very small.

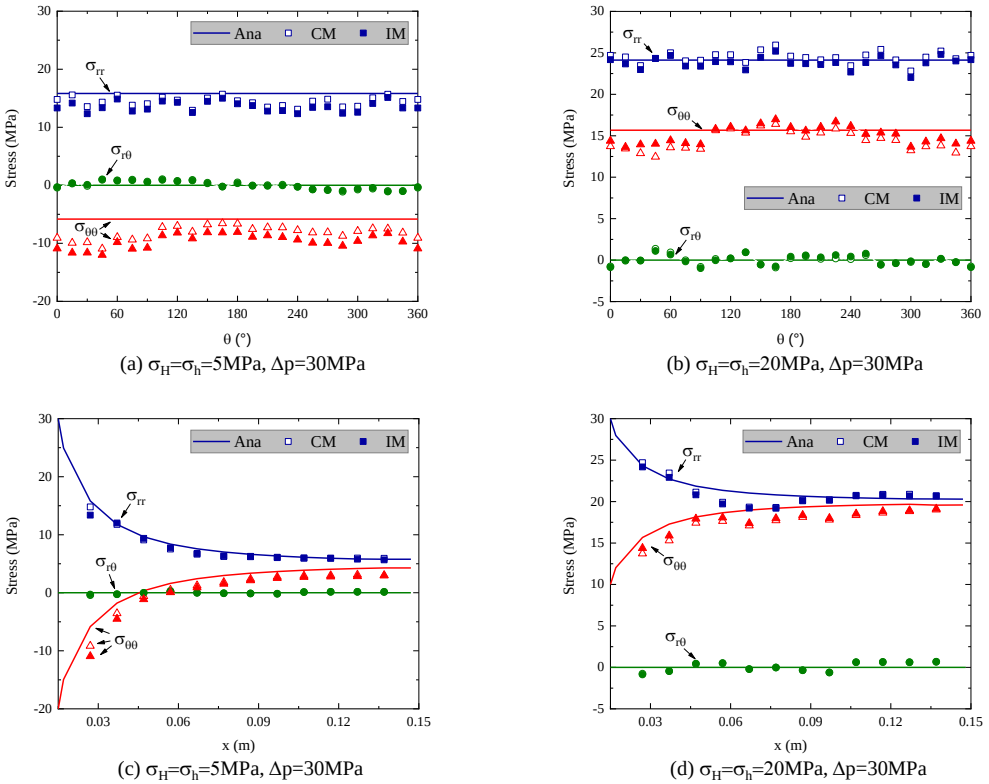

(a) σ_H=σ_h=5MPa, Δp=30MPa (b) σ_H=σ_h=20MPa, Δp=30MPa

(c) σ_H=σ_h=5MPa, Δp=30MPa (d) σ_H=σ_h=20MPa, Δp=30MPa

Figure 7: Comparisons of stress distributions around borehole between improved model (IM), common model (CM) and analytical solutions

4.2. *Comparison of fracture propagation process*

In order to show the advantage of the improved model, the fracture initiation and propagation process is now investigated. For this purpose, the case of $\sigma_H = \sigma_h$ =5MPa is considered. The set of parameters used is presented in Table 1. The injection rate is set to $1{\cdot}10^{-5}$ m^3/s.

In Fig. 8, one shows the variations of borehole pressure and induced crack number with injection time, respectively obtained from the improved (IM) and common (CM) models. The difference of results between the two models is very significant. The improved model is able to reproduce the four distinct stages such as the fracture initiation, breakdown, fracture propagation and breakthrough. On contrary, the common model provides a continuous increase of injection pressure. Further, the number of induced cracks is clearly higher in the CM than in the IM. In order to better understand such a difference, in particular the fact that the CM model produces more cracks than the IM one, the fracture initiation and propagation patterns are presented in Fig. 9 for the two models. The fracture patterns are here illustrated through the distributions of fluid pressure. Induced fractures are represented by narrow concentration zones of high fluid pressure. One can see that as for the borehole pressure evolution, the fracturing patterns are also very different between two models. With the improved model, a clearly

localized fracture is obtained. With the common model, a diffuse fractured zone around the borehole is created and multiple disordered fractures are generated beyond that zone. The difference of results is due to the fact that the fluid diffusion inside and along fractures is better described in the improved model than in the common one. As a consequence, the fluid pressure variation due to injection is concentrated around the borehole instead of going far along localized fractures. Similar results have been obtained with the common model in previous studies (Wang et al., 2014, 2017; Chong et al., 2017).

In addition, there is also a crucial difference between two models on the numerical implementation scheme of hydraulic networks. For the common model, hydraulic pipes (green ones in Fig. 9(c)) are generally directly generated with the help of contact bonds networks which are updated when a number of bonds are broken and vanish. This will hinder fluid flow between domains and along fractures. As a result, the fracture propagation is mainly driven by the continuous increment of borehole pressure. Such shortcomings have already outlined in previous works (Wang et al., 2014; Chong et al., 2017; Duan et al., 2018). For the implementation of the improved model, the hydraulic pipes networks are reconstructed after the bond breakage in order to ensure the connectivity of pipes with domains (green ones in Fig. 9(f)) before and after the bond breakage. The fracture propagation is controlled not only by the injected borehole pressure but also by the fluid pressure diffusion along generated fractures.

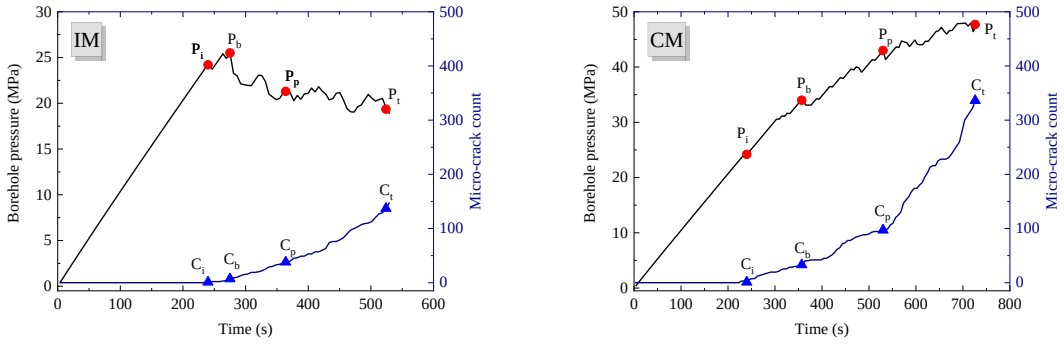

Figure 8: Evolution of borehole pressure and cracks number with fluid injection time: comparison between the improved (IM) and common model (CM)

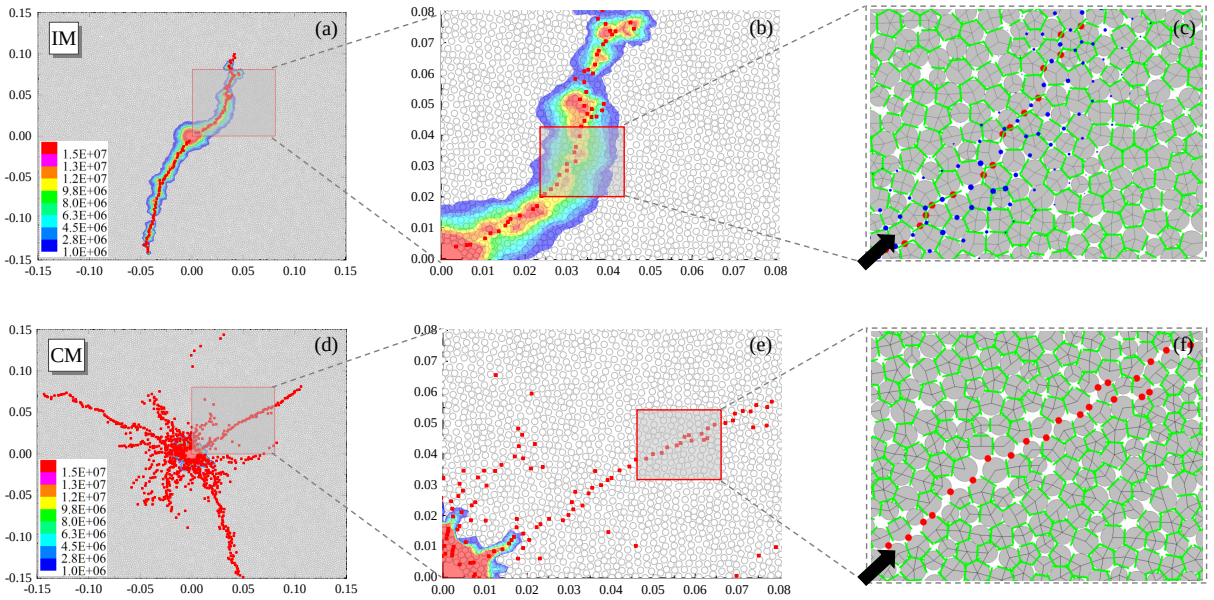

Figure 9: Distributions of fluid pressure used to illustrate fracture propagation patterns, fractures represented by red fluid pressure concentration zones: comparison between the improved (IM) and common model (CM)

5. Further investigation and sensitivity study

In this section, an additional series of numerical simulations are presented for the typical example of hydraulically-driven fracturing around a borehole considered above. The objective is to bring a more detailed analysis of fracturing process and to identify the influences of some key factors such as confining stress, fluid viscosity and injection rate. The set of parameters used and geometrical domain considered remain the same as those presented above.

5.1. Progressive fracturing process

A reference case is first considered with a confining pressure of 10 MPa and a fluid injection rate of $1{\cdot}10^{-5}$ m^3/s.

The borehole pressure evolution with injection time is presented in Fig. 10. Again, the three typical phases are well predicted by the proposed model, i.e. the fracture initiation, breakdown and propagation. The number of broken bonds is also given in this figure. It is seen that after the breakdown state, the fracture propagation continues to progress and leads to fluctuating decrease of injection pressure. In Fig. 11, one shows the fracture propagation patterns at the four characteristic values of injection pressure, in terms of fluid pressure (a to d) and contact force (e to h) distributions. One can see that a small diffuse cracked zone is first formed around the injection borehole at $p = P_i$. A first localized fracture is found when $p = P_b$. This fracture continues to propagate in an inclined direction between P_b and P_t. At $p = P_t$, the localized fracture almost reaches the external boundary of plate. Again, this type of localized fracture propagation pattern is strongly driven by the fluid pressure

diffusion along the fracture with the help of the improved hydraulic model. Further, there is a good consistency between the localized fluid pressure evolution and contact force distribution. Due to the high increase of fluid pressure, significant tensile contact forces are obtained inside the cracked zone. Therefore, it seems that the fracture propagation is here driven by the tensile cracking mechanism.

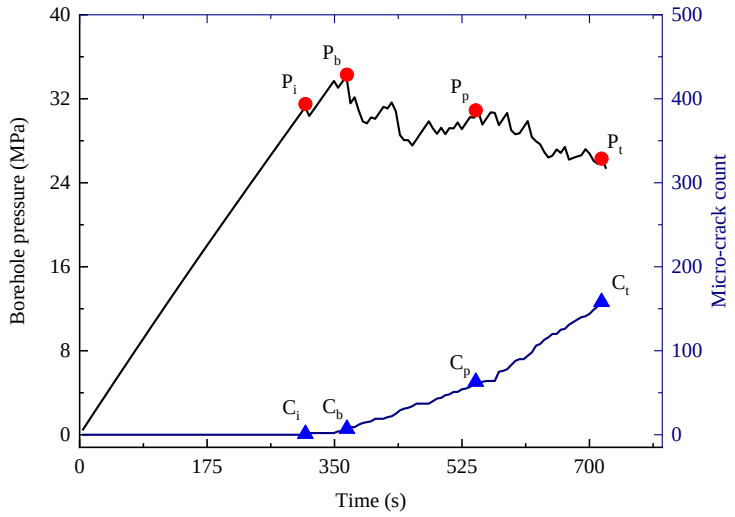

Figure 10: Borehole pressure evolution with injection time

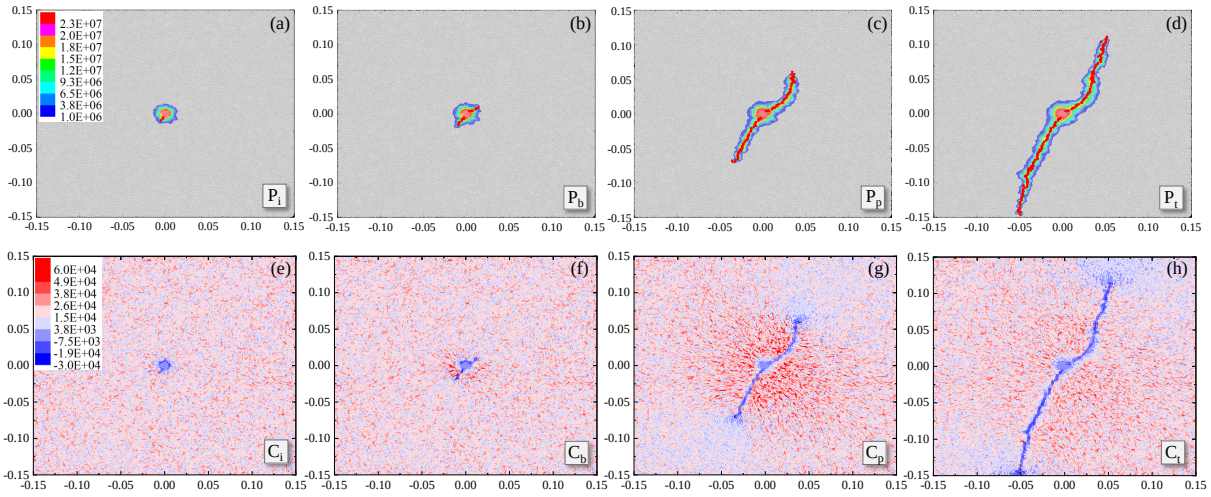

Figure 11: Distributions of fluid pressure and contact force at different instances to illustrate initiation and propagation of fractures, represented by high fluid pressure zones and low contact zones

In order to get a quantitative analysis, the distributions of three stress components around the borehole are also calculated and presented in Fig. 12, with the help of calculation circles defined in Fig. 6 and for four stages of injection pressure. It is found that at $p = P_i$ and $p = P_b$, as only quasi circular and limited cracked zones are formed, the stress distributions are almost uniform along the circumferential angle θ. Further, there is no significant differences between the two instances $p = P_i$ and $p = P_b$. However, the stress concentration begins at $p = P_b$, in particular for σ_{rr} and $\sigma_{\theta\theta}$ around

the angles 45° and 240°. After the breakdown pressure $p = P_b$, a localized fracture propagates along some privileged orientations, i.e. 45° and 240°. As a consequence, the stress distributions become more and more non-uniform and strong fluctuations are induced along θ. Significant values of the shear stress $\sigma_{r\theta}$ are also obtained. Therefore, the orientated fracture propagation patterns are closely consistent with the stress distributions.

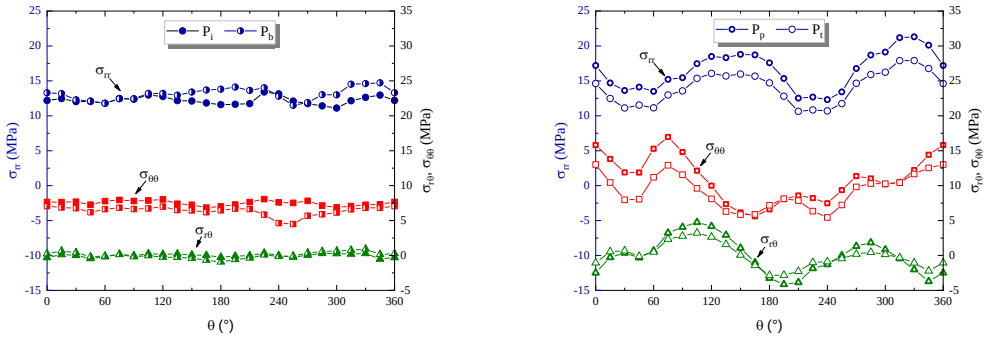

Figure 12: Local stress distributions around borehole at different representative pressure points

5.2. *Effect of confining stress*

Fracture patterns can be influenced by confining stress. In order to investigate this effect, additional simulations are here performed by taking different values of confining stress ranging from 1 MPa to 30 MPa. All other input parameters remain unchanged. Selected comparative results are presented in Fig. 13. The evolution of injection pressure with time is shown in Fig. 13 (a). One can see that the general trend is almost the same for all values of confining stress. But the different characteristic values of pressure, in particular P_b, are significantly enhanced by the confining stress. In Fig. 13 (b), it is shown that the values of P_i and P_b increase almost linearly with the confining stress. At the same time, the number of bond cracks at the fracture initiation P_i and at the breakthrough P_t also increase with the confining stress. That means that more micro-cracks are needed for generate the onset of macroscopic fractures when the confining stress is higher. In Fig. 13 (c), one compares the numerical values of breakdown pressure P_b with those calculated from the analytical estimation (Hubbert and Willis, 1957, 1972; Duan et al., 2018). According to that estimation, in the case of fluid injection into a borehole in an impermeable elastic rock, by assuming that the fracture initiation occurs when the maximum tangential stress is equal to the tensile strength of material, the breakdown injection pressure is equal to $P_b = T + 3\sigma_h - \sigma_H + P_0$, with T being the tensile strength and P_0 initial pore pressure. By using the value of T obtained from the simulation of uniaxial tension test and setting $P_0 = 0$, the value of P_b is here calculated for each confining stress $\sigma_h = \sigma_H$. It is found that there is a good agreement between the numerical and analytical results. This seems to indicate that at the stage of fracture breakdown, the fluid flow process is still moderate and the fracture initiation is

mainly driven by the initial stress, injection pressure and tensile strength of rock.

On the other hand, the propagation pattern of localized fracture is also affected by confining stress, as shown in Fig. 13 (d) in terms of fluid pressure distribution. In consistency with the variation of breakdown pressure, when the confining stress is low, the fracture initiation occurs after a short time of injection and the resulted borehole pressure is low. When the confining stress is higher, the injection time needed to create the fracture initiation is longer and the related fluid pressure is larger. Some qualitatively similar results have been reported in previous studies (Zhou et al., 2016; Duan et al., 2018). Moreover, it seems that the fluid flow along the localized fracture itself plays a more important role under a high confining stress than a low one. As a consequence, one obtains a slightly narrower fractured zone.

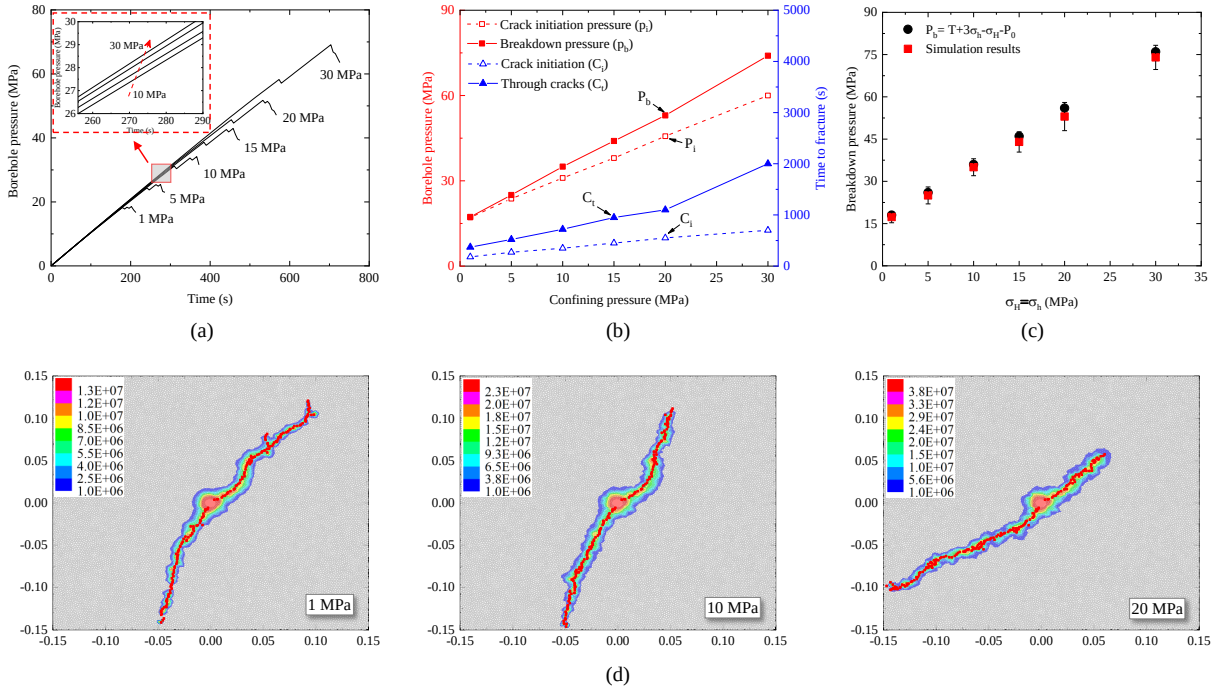

Figure 13: Selected results of simulations with different confining stresses: (a) Borehole pressure with time; (b) Variations of characteristic pressures and micro-cracks numbers with confining stress; (c) Comparison between numerical and theoretical results; (d) Fluid pressure distribution used to show fracture propagation patterns, fractures represented by high fluid pressure zones

5.3. Effect of fluid injection rate

In this section, the effects of fluid injection rate on fracturing process are investigated. In particular, the dependence of breakdown pressure upon the rate of borehole pressurization is analyzed. For this purpose, a series of simulations are performed with different fluid injection rates ranging from $1{\cdot}10^{-6}$ m^3/s to $1{\cdot}10^{-4}$ m^3/s, and under two confining stresses of 1MPa and 20MPa. Other parameters remain unchanged.

The results on the borehole pressure and micro-cracks count are presented in Fig. 14 (a) and (b). It is seen that the general shape of pressure curve is almost the same for all injection rates. The value of breakdown pressure P_b exhibits a sharp drop from the rate of $1{\cdot}10^{-4}$ m^3/s to $2.5{\cdot}10^{-5}$ m^3/s ($5{\cdot}10^{-6}$ m^3/s for the confining stress of 20MPa) and then remains almost constant when the injection rate is lower. However, the slope of pressure curve before fracture initiation point continuously decreases when the injection rate is lower. Very similar results are obtained for two confining stresses. At the same time, the number of micro-cracks induced at $p = P_b$ is significantly reduced from the rate of $1{\cdot}10^{-4}$ m^3/s to $2.5{\cdot}10^{-5}$ m^3/s and tends towards a stationary value when the injection rate is lower.

For a more quantitative analysis, the values of P_i and P_b and the time needed to reach the stages of P_i and P_t are expressed as functions of fluid injection rate in Fig. 15. It is obvious that their values suddenly increase when the injection rate is higher than $1.5{\cdot}10^{-5}$ m^3/s for 1 MPa confining stress and a bit lower value for 20 MPa. The increase of P_b is more significant than that of P_t. However, the time needed to reach the fracture initiation and breakthrough decreases first quickly and then slowly with the increase of injection rate.

It seems that there exists a critical value of fluid injection rate below which its effect on fracturing process becomes negligible. When the fluid injection rate is higher than this critical value, due to the hydrodynamic effect of quick fluid pressure increase, a larger number of micro-cracks are created before the fracture breakdown is reached.

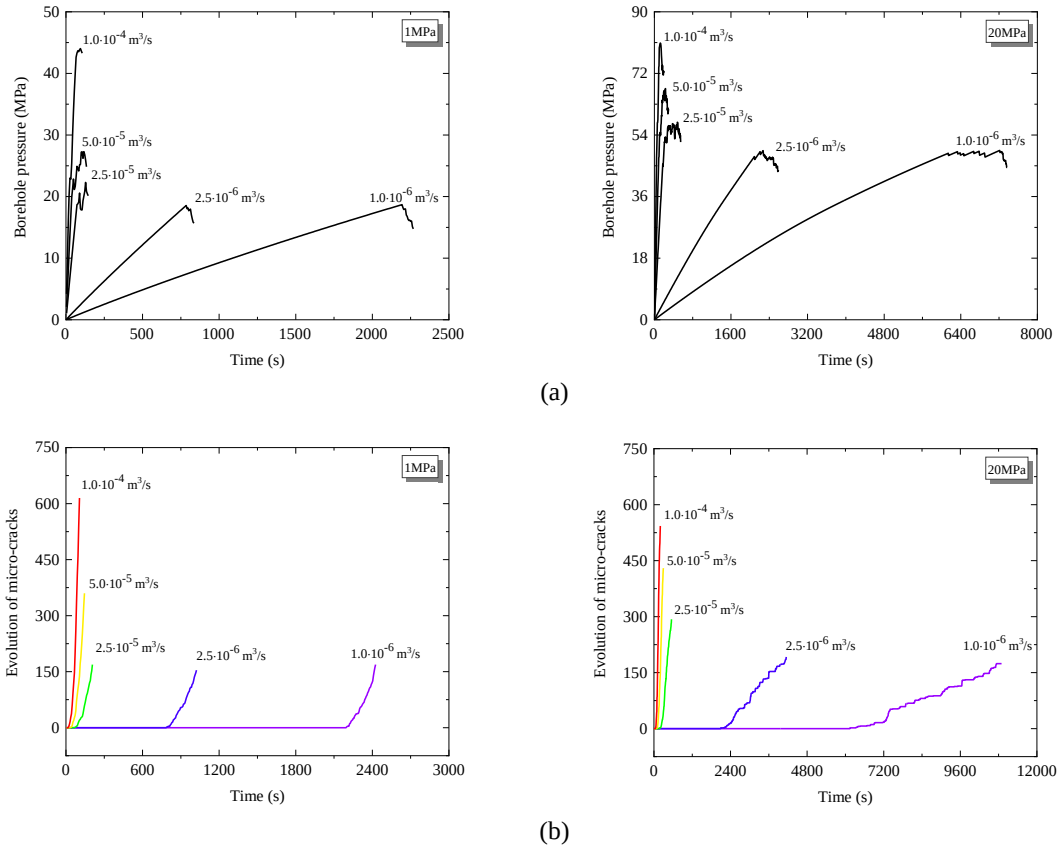

Figure 14: Evolution of borehole pressure (a) and micro-cracks number (b) with time for six values of fluid injection rate

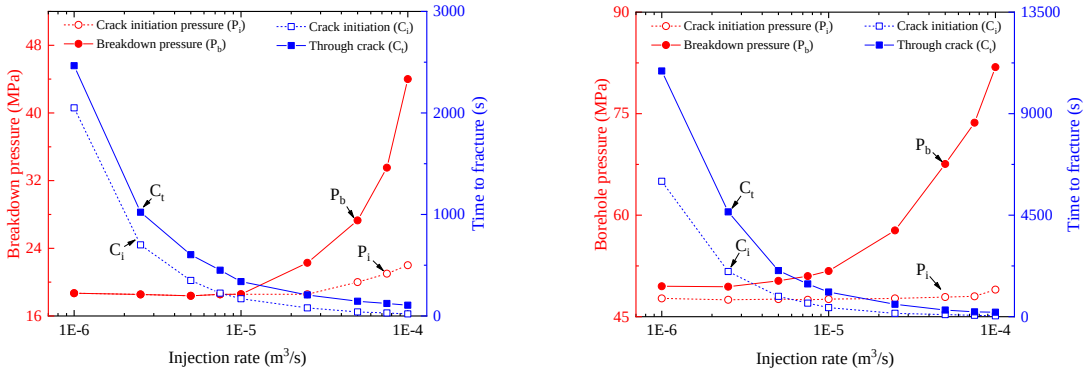

Figure 15: Variations of P_i and P_b with injection rate and time needed to reach P_i and P_t for confining stresses of 1 MPa (left) and 20 MPa (right)

The fracture propagation patterns for different injection rates are presented in Fig. 16 in terms of fluid pressure distribution. For both low and high confining stresses, the fracture pattern is influenced by the injection rate. In a general way, when the injection rate is low, a large and circular pressure diffusion zone is generated by fluid injection. This zone propagates in some orientations. The fracture propagation is accompanied by the fluid diffusion into porous rock matrix. The width of pressure diffusion zone is larger when the injection rate is lower. On contrary, under a high injection rate, the fluid diffusion into rock matrix is negligible. The fracture initiation occurs in a sudden manner and its

propagation is essentially driven by the fluid transport along fractures. When the injection rate is high enough, multiple fractures can initiate and propagate simultaneously in different orientations. This change of fracture propagation patterns as well as fluid pressure distribution is observed in both low and high confining stress.

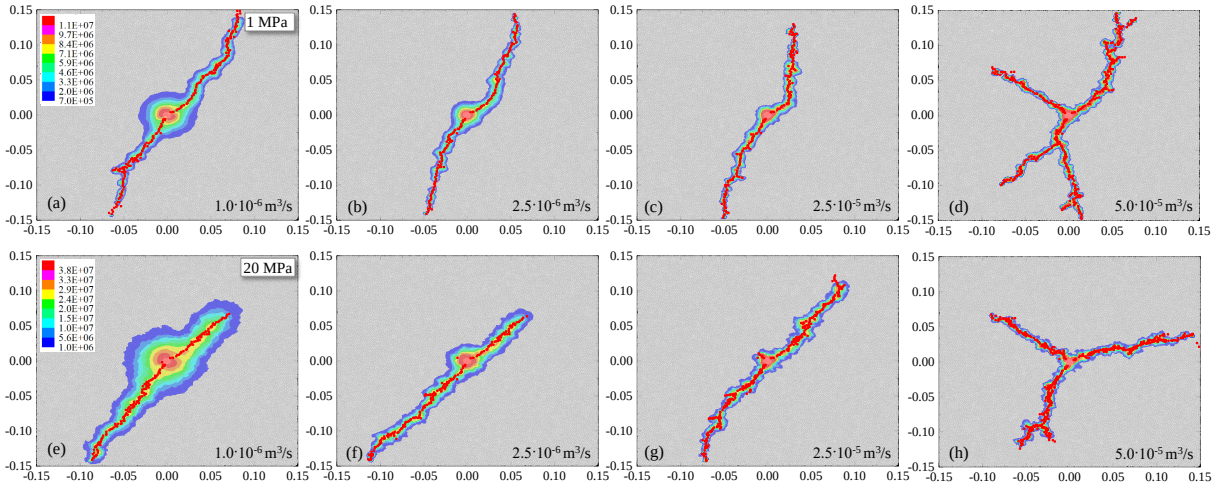

Figure 16: Distributions of fluid pressure used to illustrate fracture propagation patterns for different fluid injection rates under two confining stresses of 1MPa and 20MPa, fractures represented by high fluid pressure zones

5.4. *Effect of fluid viscosity*

Fluid viscosity affects the kinetics of fluid diffusion and accordingly the fracturing process (Shimizu et al., 2011; Zhang et al., 2017). In this section, the effects of fluid viscosity on pore pressure distribution and fracturing pattern are investigated. To this end, a series of simulations are carried out by considering different values of fluid viscosity between $1{\cdot}10^{-4}$ Pa.s and $1{\cdot}10^{-2}$ Pa.s, and for two confining stresses of 1MPa and 20 MPa. The injection rate is set to $1{\cdot}10^{-5}$ m^3/s.

In Fig. 17(a) and (b), one shows the evolution curves of borehole pressure and induced microcracks count for some selected values of viscosity. The variations with fluid viscosity of P_i (fracture initiation pressure) and P_b (breakdown pressure) as well as those of the time needed to reach the fracture initiation (C_i) and breakthrough (C_t) are presented in Fig. 18. It is found that the slope of pressure curve before the fracture initiation increases with the raise of fluid viscosity. This logically indicates that the setup of pore pressure is easier when the injected fluid is more viscous. Accordingly, the values of two characteristic pressures, i.e. P_i and P_b, are also raised when the fluid viscosity is higher. However, the impact is much more significant for P_b than for P_i. At the same time, the time needed to reach the crack initiation and the breakthrough is significantly reduced. Therefore, when a fluid with heavy viscosity is injected, a short time is needed to generate localized fracture breakthrough but this is compensated by a high breakdown pressure. The presented numerical results

seem to be in agreement with experimental data in similar situations (Zhang et al., 2017), and the present hydromechanical model improves some previous numerical studies (Ishida et al., 2004).

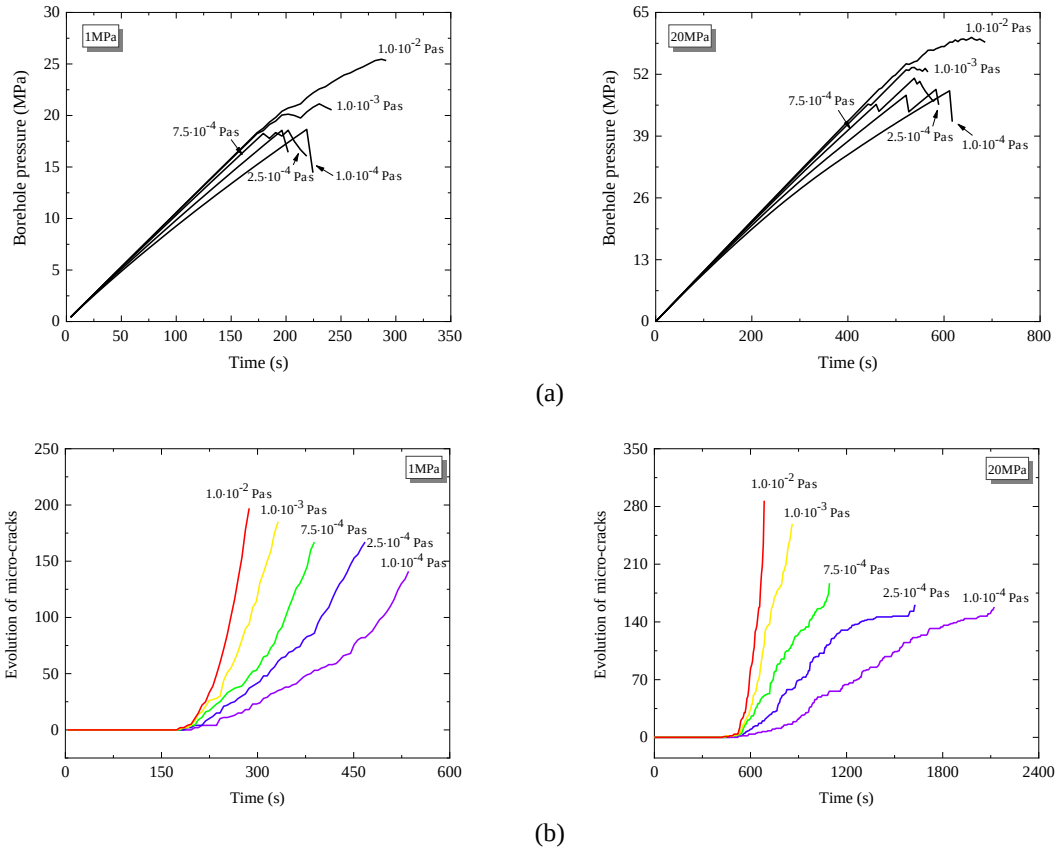

Figure 17: Evolution of borehole pressure (a) and micro-cracks count (b) for different values of fluid viscosity and under confining stresses of 1 MPa (left) and 20 MPa (right)

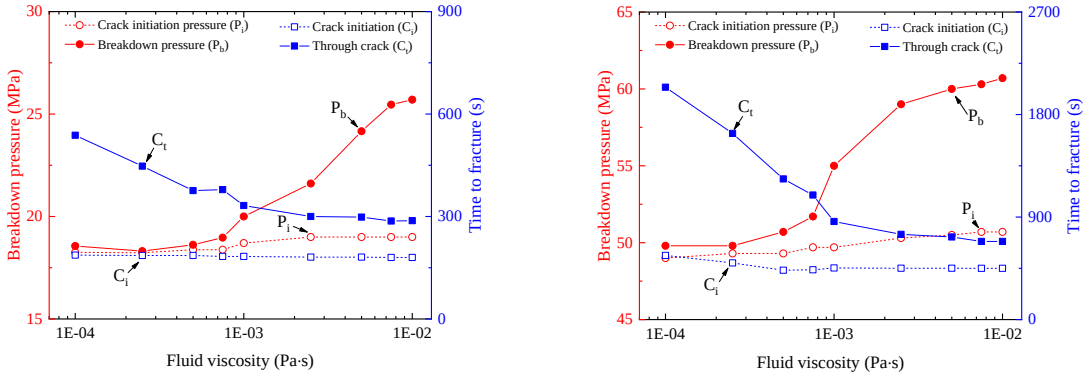

Figure 18: Variations with fluid viscosity of P_i and P_b and of time needed to reach crack initiation C_i and breakthrough C_t for confining stresses of 1 MPa (left) and 20 MPa (right)

In Fig. 19, we show the fracture patterns for two selected values of fluid viscosity (low and high) in terms of pore pressure for two representative stages (P_p, P_t). It is obvious that the fracture pattern is strongly influenced by the fluid viscosity. As expected, for the low viscous fluid, the diffusion

into porous rock matrix is easy. One obtains a very large pressure diffusion zone. On contrary, for the fluid with a high viscosity, the infiltration into the porous rock matrix is not significant and the pressure diffusion is limited into narrow bands around through-fractures. The fracture propagation is clearly driven by the fluid transport inside the fractures. Further, under a low confining stress, several secondary fractures can be created from the main one.

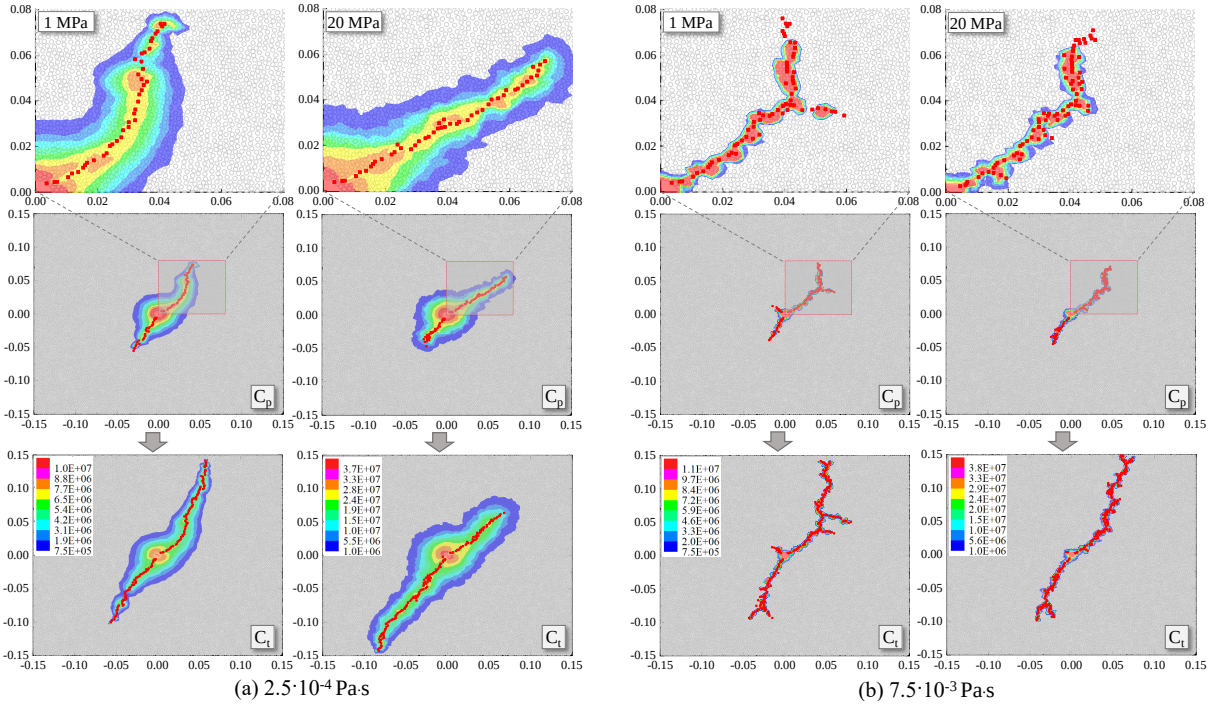

(a) $2.5 \cdot 10^{-4}$ Pa·s (b) $7.5 \cdot 10^{-3}$ Pa·s

Figure 19: Fracture propagation patterns in terms of fluid pressure distribution for low and high fluid viscosity under two confining stresses of 1 MPa and 20 MPa at the stages of fracture breakdown (C_p, second row) and breakthrough (C_t, third row)

6. Discussion

In the previous sections, the efficiency of the particle simulation based method in modeling cracking process in fluid-saturated rocks has been illustrated by using the improved hydro-mechanical model. Compared with continuum-mechanics based methods such as extended finite element method (we do not give here an exhaustive list of many papers on the subject), it is not needed to define specific criteria for the onset and propagation description of fractures. The macroscopic cracking process is physically related to the microscopic breakage of cohesive contacts between particles. At the same time, the hydromechanical coupling process is also directly taken into account at the pore scale by considering fluid mass change between pores and pipes. Furthermore, the transition from diffuse micro-cracks to localized macro-fractures is naturally described with any additional criteria

and numerical treatments. The particle simulation based method is also efficient for modeling the onset and propagation of multiple fractures.

However, the key parameters involved in the particle simulation method are defined at the scale of grains and contacts. In general, they cannot be directly determined from macroscopic laboratory tests. Suitable procedures should be developed for the determination of such microscopic parameters. The setup of initial and boundary conditions is also a delicate task in the particle simulation based method. Moreover, as already mentioned above, for real engineering applications, it is needed to take into account multi-physical and chemical processes (Zhao et al., 2008b,c, 2010). Compared with classical continuum based methods, the description of such processes is so far delicate to complete with the particle simulation based method. Further theoretical and numerical studies should be performed on this issue. Furthermore, numerical predictions with the particle simulation method can depend on size and shape of particles. The computing time can significantly increase with a high number of particles. Therefore, a suitable combination of continuum and particle simulation based methods provides an interesting perspective.

7. Conclusions

In the paper, we have proposed an improved hydromechanical coupling model in the framework of particle flow method in order to better describe the evolution of hydraulic pipe aperture with micro-structural change before and after the breakage of contact bonds. This model also takes into account the instantaneous fluid pressure equilibrium between two neighboring domains due to the bond breakage.

The efficiency of the improved model has been assessed by the comparisons with the analytical solutions on the stress distribution around borehole and some commonly observed experimental evidences. In particular, with the new model, it is possible to capture all different stages of borehole pressure evolution during an injection test, namely the fracture initiation, breakdown, fracture propagation and breakthrough. The description of localized fracture patterns is also significantly improved. It is found that the fluid diffusion inside localized fractures can play a dominant role on their propagation pattern.

A series of sensitivity studies have been further presented. It has been clearly shown that both the borehole pressure evolution and fracturing pattern were influenced by confining stress, fluid injection rate and viscosity. Under a high confining stress, a large number of bonds are broken before the onset of localized fracture breakthrough. When the fluid injection rate is high, the breakdown pressure is significantly increased and there is a possibility to create multiple localized fractures. The fracture breakdown pressure decreases when the fluid viscosity is lower but the time needed to reach the

fracture breakthrough is longer, due to the important infiltration of fluid into the porous rock matrix.

Structural anisotropy of rocks should play an important role in deformation and fracturing process. The present work can be easily extended to such anisotropic rocks in future studies.

Acknowledgment

This study has been jointly supported by the State Key RD Program of China (Grant 2017YFC1501100), China Postdoctoral Science Foundation (Grant 2019TQ0080, Grant 2020M671320), and the Key Laboratory of Ministry of Education on Safe Mining of Deep Metal Mines (Grant DM2019K02).

References

References

Al-Busaidi, A., Hazzard, J., Young, R., 2005. Distinct element modeling of hydraulically fractured lac du bonnet granite. Journal of Geophysical Research: Solid Earth 110.

Ambati, M., Gerasimov, T., De Lorenzis, L., 2015. A review on phase-field models of brittle fracture and a new fast hybrid formulation. Computational Mechanics 55, 383–405.

Ambrosio, L., Tortorelli, V.M., 1990. Approximation of functional depending on jumps by elliptic functional via t-convergence. Communications on Pure and Applied Mathematics 43, 999–1036.

Bohloli, B., de Pater, C., 2006. Experimental study on hydraulic fracturing of soft rocks: Influence of fluid rheology and confining stress. Journal of Petroleum Science and Engineering 53, 1–12.

Borden, M.J., Verhoosel, C.V., Scott, M.A., Hughes, T.J., Landis, C.M., 2012. A phase-field description of dynamic brittle fracture. Computer Methods in Applied Mechanics and Engineering 217, 77–95.

Bourdin, B., Francfort, G.A., Marigo, J.J., 2000. Numerical experiments in revisited brittle fracture. Journal of the Mechanics and Physics of Solids 48, 797–826.

Chong, Z., Karekal, S., Li, X., Hou, P., Yang, G., Liang, S., 2017. Numerical investigation of hydraulic fracturing in transversely isotropic shale reservoirs based on the discrete element method. Journal of Natural Gas ence and Engineering , S1875510017303384.

Choo, J., Sun, W., 2018. Coupled phase-field and plasticity modeling of geological materials: From brittle fracture to ductile flow. Computer Methods in Applied Mechanics and Engineering 330, 1–32.

Cundall, P., 2008. Pfc2d user's manual (ver 4.0). Minnesota: Itasca Consulting Group Inc .

Damjanac, B., Cundall, P., 2016. Application of distinct element methods to simulation of hydraulic fracturing in naturally fractured reservoirs. Computers and Geotechnics 71, 283–294.

Duan, Kang, Kwok, Chung, Yee, Wu, Wei, Jing, Lu, 2018. Dem modeling of hydraulic fracturing in permeable rock: influence of viscosity, injection rate and in situ states. Acta Geotechnica An International Journal for Geoengineering .

Eshiet, K.I., Sheng, Y., Ye, J., 2013. Microscopic modelling of the hydraulic fracturing process. Environmental earth sciences 68, 1169–1186.

Fang, J., Wu, C., Li, J., Liu, Q., Wu, C., Sun, G., Qing, L., 2019. Phase field fracture in elasto-plastic solids: variational formulation for multi-surface plasticity and effects of plastic yield surfaces and hardening. International Journal of Mechanical Sciences .

Fatahi, H., Hossain, M.M., Sarmadivaleh, M., 2017. Numerical and experimental investigation of the interaction of natural and propagated hydraulic fracture. Journal of Natural Gas Science and Engineering 37, 409–424.

Francfort, G.A., Marigo, J.J., 1998. Revisiting brittle fracture as an energy minimization problem. Journal of the Mechanics and Physics of Solids 46, 1319–1342.

Goodfellow, S.D., Nasseri, M.H.B., Maxwell, S.C., Young, R.P., 2015. Hydraulic fracture energy budget: Insights from the laboratory. Geophysical Research Letters 42, 3179–3187.

Haimson, B., 2007. Micromechanisms of borehole instability leading to breakouts in rocks. International Journal of Rock Mechanics and Mining Sciences 44, 157–173.

Haimson, B., Cornet, F., 2003. Isrm suggested methods for rock stress estimation, part 3: hydraulic fracturing (hf) and/or hydraulic testing of pre-existing fractures (htpf). International Journal of Rock Mechanics and Mining Sciences 40, 1011–1020.

Hubbert, M.K., Willis, D.G.W., 1957. Mechanics of hydraulic fracturing. Trans. Am. Inst. Min. Eng. 210, 153–168.

Hubbert, M.K., Willis, D.G.W., 1972. Mechanics of hydraulic fracturing. Developments in Petroleum Science 18, 369–390.

Ishida, T., Chen, Q., Mizuta, Y., Roegiers, J.C., 2004. Influence of fluid viscosity on the hydraulic fracturing mechanism. Journal of Energy Resources Technology 126, 190–200.

Jian, Z., Yan, J., Chen, M., 2010. Experimental investigation of hydraulic fracturing in random naturally fractured blocks. International Journal of Rock Mechanics and Mining Sciences 47, 1193–1199.

Kirsch, C., 1898. Die theorie der elastizitat und die bedurfnisse der festigkeitslehre. Ztschrift des Vernes Deutscher Ingenieure 42, 797–807.

Miehe, C., Hofacker, M., Schänzel, L.M., Aldakheel, F., 2015. Phase field modeling of fracture in multi-physics problems. part ii. coupled brittle-to-ductile failure criteria and crack propagation in thermo-elastic–plastic solids. Computer Methods in Applied Mechanics and Engineering 294, 486–522.

Miehe, C., Hofacker, M., Welschinger, F., 2010. A phase field model for rate-independent crack propagation: Robust algorithmic implementation based on operator splits. Computer Methods in Applied Mechanics and Engineering 199, 2765–2778.

Moes, N., Dolbow, J., Belytschko, T., 1999. A finite element method for crack growth without remeshing. Internat. J. Numer. Methods Engrg. 46, 131–150.

Mumford, D., Shah, J., 1989. Optimal approximations by piecewise smooth functions and associated variational problems. Communications on pure and applied mathematics 42, 577–685.

Nazari Moghaddam, R., Jamiolahmady, M., 2016. Fluid transport in shale gas reservoirs: Simultaneous effects of stress and slippage on matrix permeability. International Journal of Coal Geology 163, 87–99.

Oliver, J., 1996. Modelling strong discontinuities in solid mechanics via strain softening constitutive equations, part 1: fundamentales. Internat. J. Numer. Methods Engrg. 39, 3575–3600.

Potyondy, D., Cundall, P., 2004. A bonded-particle model for rock. International journal of rock mechanics and mining sciences 41, 1329–1364.

Pruess, K., 2006. Enhanced geothermal systems (egs) using co2 as working fluid, a novel approach for generating renewable energy with simultaneous sequestration of carbon. Geothermics 35, 351–367.

Sarmadivaleh, M., Rasouli, V., 2015. Test design and sample preparation procedure for experimental investigation of hydraulic fracturing interaction modes. Rock Mechanics and Rock Engineering 48, 93–105.

Shimizu, H., Murata, S., Ishida, T., 2011. The distinct element analysis for hydraulic fracturing in hard rock considering fluid viscosity and particle size distribution. International Journal of Rock Mechanics and Mining Sciences 48, 712–727.

Wang, T., Hu, W., Elsworth, D., Zhou, W., Zhou, W., Zhao, X., Zhao, L., 2017. The effect of natural fractures on hydraulic fracturing propagation in coal seams. Journal of Petroleum Science and Engineering 150, 180–190.

Wang, T., Zhou, W.B., Chen, J.H., Xiao, X., Li, Y., Zhao, X.Y., 2014. Simulation of hydraulic fracturing using particle flow method and application in a coal mine. International Journal of Coal Geology 121, 1–13.

Warpinski, N.R., Mayerhofer, M.J., Vincent, M.C., Cipolla, C.L., Lolon, E.P., 2009. Stimulating unconventional reservoirs: Maximizing network growth while optimizing fracture conductivity. Journal of Canadian Petroleum Technology 48, 39–51.

Worthington, P.F., 2008. A diagnostic approach to quantifying the stress sensitivity of permeability. Journal of Petroleum Science and Engineering 61, 49–57.

Zeng, Q.D., Yao, J., Shao, J.F., 2018. Numerical study of hydraulic fracture propagation accounting for rock anisotropy. Journal of Petroleum Science and Engineering 160, 422–432.

Zeng, Q.D., Yao, J., Shao, J.F., 2019. Study of hydraulic fracturing in an anisotropic poroelastic medium via a hybrid edfm-xfem approach. Computers and Geotechnics 105, 51–68.

Zhang, X., Lu, Y., Tang, J., Zhe, Z., Yin, L., 2017. Experimental study on fracture initiation and propagation in shale using supercritical carbon dioxide fracturing. Fuel 190, 370–378.

Zhang, Y.L., Shao, J.F., Liu, Z.B., Shi, C., De Saxce, G., 2018. Effects of confining pressure and loading path on deformation and strength of cohesive granular materials: a three-dimensional dem analysis. Acta Geotechnica 14, 443–460.

Zhang, Y.L., Shao, J.F., de Saxce, G., Shi, C., Liu, Z.B., 2019. Study of deformation and failure in an anisotropic rock with a three-dimensional discrete element model. International Journal of Rock Mechanics and Mining ences 120, 17–28.

Zhao, Chongbin, B., E., Hobbs, A., Ord, 2010. Theoretical analyses of nonaqueous phase liquid dissolution-induced instability in two-dimensional fluid-saturated porous media. International Journal for Numerical and Analytical Methods in Geomechanics 34, 1767–1796.

Zhao, Chongbin, B., E., Hobbs, A., Ord, Shenglin, Peng, 2008a. Particle simulation of spontaneous crack generation associated with the laccolithic type of magma intrusion processes. International Journal for Numerical Methods in Engineering 75, 1172–1193.

Zhao, C., Hobbs, B.E., Hornby, P., Ord, A., Liu, L., 2008b. Theoretical and numerical analyses of chemical-dissolution front instability in fluid-saturated porous rocks. International Journal for Numerical and Analytical Methods in Geomechanics 32, 1107–1130.

Zhao, C., Hobbs, B.E., Ord, A., 2008c. Convective and Advective Heat Transfer in Geological Systems. Convective and Advective Heat Transfer in Geological Systems.

Zhao, C., Hobbs, B.E., Ord, A., 2009. Fundamentals of computational geoscience numerical methods and algorithms. Lecture Notes in Earth Sciences .

Zhao, C., Hobbs, B.E., Ord, A., Hornby, P., Peng, S., Liu, L., 2007. Particle simulation of spontaneous crack generation problems in large-scale quasi-static systems. International Journal for Numerical Methods in Engineering 69, 2302–2329.

Zhao, X., 2010. Imaging the mechanics of hydraulic fracturing in naturally-fractured reservoirs using induced seismicity and numerical modeling. Thesis Ph.D. University of Toronto, Canada .

Zhou, J., Chen, M., Jin, Y., Zhang, G.q., 2008. Analysis of fracture propagation behavior and fracture geometry using a tri-axial fracturing system in naturally fractured reservoirs. International Journal of Rock Mechanics and Mining Sciences 45, 1143–1152.

Zhou, J., Luqing, Z., Pan, Z., Han, Z., 2016. Numerical investigation of fluid-driven near-borehole fracture propagation in laminated reservoir rock using pfc2d. Journal of Natural Gas Science and Engineering 36, 719–733.

Zisser, N., Nover, G., 2009. Anisotropy of permeability and complex resistivity of tight sandstones subjected to hydrostatic pressure. Journal of Applied Geophysics 68, 356–370.

Zoback, M., Rummel, F., Jung, R., Raleigh, C.B., 1977. Laboratory hydraulic fracturing experiments in intact and pre-fractured rock. International Journal of Rock Mechanics and Mining Sciences & Geomechanics Abstracts 14, 49–58.